Extended Abstracts of the 2006 International Conference on Solid State Devices and Materials, Yokohama, 2006, pp. 1098-1099

J-7-1

Optimization of Hafnium Zirconate ($HfZrO_x$) Gate Dielectric for Device Performance and Reliability

R. I. Hegde, D. H. Triyoso, S. Kalpat, S. B. Samavedam, J. K. Schaeffer, E. Luckowski, C. Capasso, D. C. Gilmer, M. Raymond, D. Roan, J. Nguyen, L. La, E. Hebert, X-D. Wang, R. Gregory, R. S. Rai, J. Jiang, T. Y. Luo, and B. E. White Jr.

Freescale Semiconductor, Inc., Austin Silicon Technology Solutions (ASTS), 3501 Ed Bluestein Blvd., MD: K10, Austin, TX78721, USA (Tel: 512-933-7072, Fax: 512-933-6962, Rama.Hegde@Freescale.com)

ABSTRACT

Optimization of ZrO_2 content in $HfZrO_x$ gate dielectric for transistor performance, mobility, reliability, and thermal stability is reported for the first time. Incorporation of ZrO_2 into HfO_2 enhances dielectric constant (K) of resulting $HfZrO_x$ which is associated with structural phase transformation from monoclinic to tetragonal. The tetragonal phase increases K of $HfZrO_x$ to a large value as predicted.

INTRODUCTION

Recently, a novel hafnium zirconate ($HfZrO_x$) alloy gate dielectric was developed to address the shortcomings of HfO_2 [1]. In this paper a systematic investigation was performed on the dielectric properties of $HfZrO_x$ with Ta_xC_y metal gate as a function of ZrO_2 content. Also, boost in the K value of $HfZrO_x$ dielectric is discussed.

EXPERIMENT

The integration follows a standard CMOS process flow on silicon up to $HfZrO_x$ dielectric deposition. The target 30Å ALD $HfZrO_x$ films with four different levels of ZrO_2 (zero, A, B, and C) were deposited at 300°C on RCA cleaned Si. The precursors used for ALD were $HfCl_4$, $ZrCl_4$, and D_2O. The Ta_xC_y was used as NMOS gate [2]. A commercial CMOS process technology [3] with activation anneal at 1000°C/5s/N_2 was used to fabricate metal gate/high-K stack MOSFETs.

RESULTS AND DISCUSSION

(a)Transistor Characteristics

Figure 1 shows well-behaved NMOSFET C-V characteristics of $HfZrO_x$(B) and HfO_2. Compared to HfO_2, the $HfZrO_x$(B) has a lower CET_{inv} value. The lower CET_{inv} value is due to higher K of the $HfZrO_x$(B) compared to HfO_2 as shown in Figure 2. Figure 3 plots gate leakage current density (J_g) as a function of CET_{inv}. As shown, the gate leakage for the $HfZrO_x$(B) devices is over 4 orders of magnitude lower than that of silicon oxynitride. Compared to HfO_2, slightly higher gate leakage current was observed for the $HfZrO_x$ devices. This is due to smaller band gap and lower conduction band offset for $HfZrO_x$ than that of HfO_2 [1]. The electron mobility evaluation in Figure 4 indicated ~7% increase in peak mobility and ~8% increase in mobility at large inversion (high field) for the $HfZrO_x$(B) devices compared to HfO_2 control. The hole mobility comparison in Figure 5 showed ~9% increase in peak mobility and ~7% increase in mobility at large inversion charge for $HfZrO_x$(B) devices. Thus, the $HfZrO_x$ dielectric is attractive candidate for CET_{inv} scaling for high performance and low leakage for low standby power applications. The composition optimization of $HfZrO_x$ was performed on long channel transistors fabricated using a shorter flow. Figure 6 shows Hf SIMS depth profiling from the long channel MOSFETs indicating expected levels of ZrO_2 in the $HfZrO_x$ dielectrics. The Table 1 summarizes CET_{inv}, V_t and SS values for the $HfZrO_x$ devices with different levels of ZrO_2. Compared to HfO_2, consistently lower CET_{inv} values were obtained for $HfZrO_x$ with composition A, B, and C. The K value of $HfZrO_x$ is dependent on $HfZrO_x$ composition as shown in Figure 7 and on $HfZrO_x$ structure as discussed below. In Figure 8, the I_d-V_g characteristics showed that all $HfZrO_x$ devices including HfO_2 have low SS values of 67-68mV/dec, indicating formation of high quality dielectric/Si interfaces. The cross-sectional TEM micrographs in Figure 9 showed that the $HfZrO_x$ dielectrics are polycrystalline with similar bulk dielectric thickness (26-30Å) and interfacial oxide thickness (~9Å). No interaction between the $HfZrO_x$ dielectrics and Si channel was observed after the 1000°C activation anneals. Thus, these $HfZrO_x$ dielectrics showed good thermal stability with Si. The normalized transconductance (G_m) characteristics in Figure 10 confirmed higher G_m for the $HfZrO_x$ devices compared to HfO_2. The BTI characteristics (PBTI and NBTI) for $HfZrO_x$ devices in Figures 11 and 12 showed substantial improvement with ZrO_2 content for NMOS(PMOS) at 1.5V(-2V) stress voltage, respectively. The device performance and reliability improvement is primarily attributed to tetragonal structure of $HfZrO_x$ (see below) with a lower bulk trap density [1].

(b)Boost in Dielectric Constant (K)

The K enhancement for $HfZrO_x$ in Figure 2 and 7 comes from structural phase transformation. Figure 13 shows plan view TEM and selected area electron diffraction (SAD) for 40Å HfO_2 and $HfZrO_x$(B) dielectric films after Ta_xC_y gate removal. The TEM data showed smaller and more uniform grains for $HfZrO_x$(B) compared to HfO_2, consistent with AFM images in Figure 14. The SAD data showed tetragonal grains in $HfZrO_x$(B) dielectric compared to purely monoclinic in HfO_2. Further, thin film XRD results in Figure 15 suggested presence of mainly tetragonal phase for the 40Å $HfZrO_x$(B) dielectric. The tetragonal ZrO_2 phase is theoretically predicted [4-6] to have higher dielectric constant (K~47) than monoclinic phase (K~20). The improved device characteristics are due to fine grained micro-structure of $HfZrO_x$ with increased grain boundary area that results in less oxygen vacancy. More oxygen in grain boundary will reduce equilibrium concentration of oxygen vacancy in the bulk of the grains.

CONCLUSIONS

Addition of ZrO_2 stabilizes the tetragonal phase and enhances the K value in $HfZrO_x$ devices. The ZrO_2 content needs to be optimized for performance. The $HfZrO_x$ dielectric is an attractive candidate for advanced gate stack applications.

ACKNOWLEDGEMENT

The authors would like to thank Suresh Venkatesan, Director of ASTS, for management support.

REFERENCES

[1] R. I. Hegde, et al, IEDM, p.39 (2005)
[2] J. K. Schaeffer, et al, IEDM p.287 (2004)
[3] A. Perera, et al, IEDM, p.571 (2000)
[4] H. Kim, et al, J. Mater. Res. **20**, 3125 (2005)
[5] S. Sayan, et al, App. Phys. Letters **86**, 152902 (2005)
[6] X. Zhao, et al, Phys. Rev. B **65**, 075105 (2002)

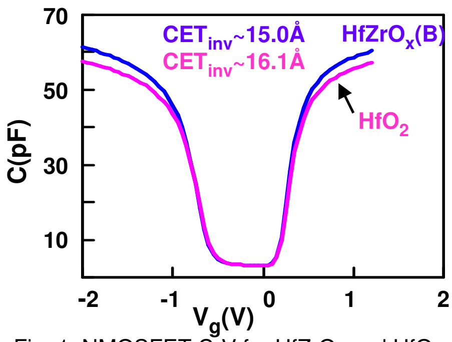

Fig. 1 NMOSFET C-V for $HfZrO_x$ and HfO_2 (W/L=10µmX10µm)

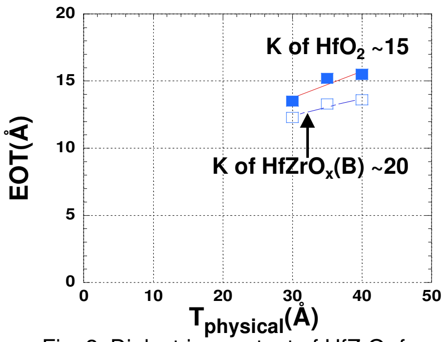

Fig. 2 Dielectric constant of $HfZrO_x$ from EOT vs. physical thickness

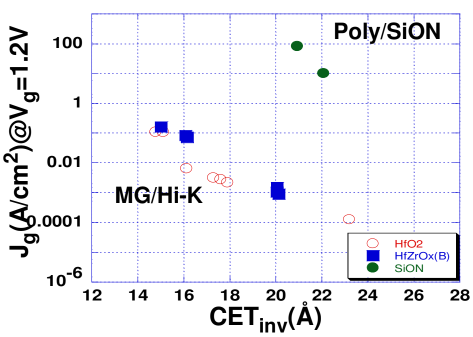

Fig. 3 Gate leakage current density as a function of CET_{inv}

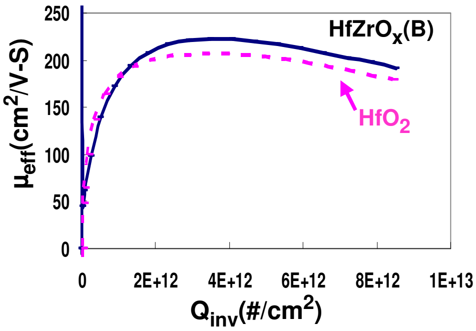

Fig. 4 Electron mobility for HfO_2 and $HfZrO_x$ devices (W/L=10umX10um)

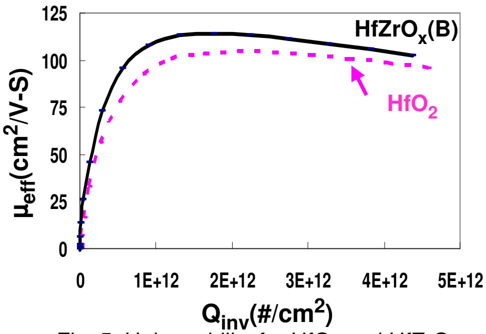

Fig. 5 Hole mobility for HfO_2 and $HfZrO_x$ devices (W/L=10umX10um)

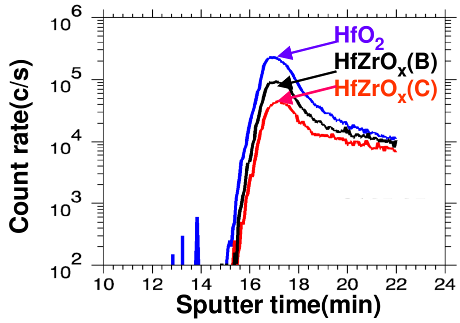

Fig. 6 Hf SIMS depth profiling from $HfZrO_x$ MOSFETs

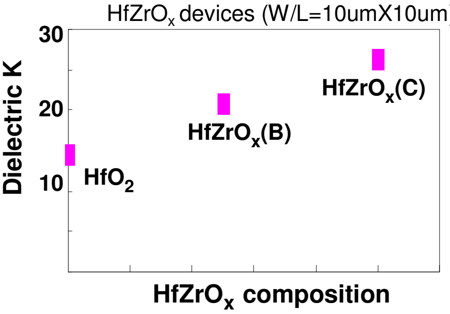

Fig. 7 K value vs. $HfZrO_x$ composition

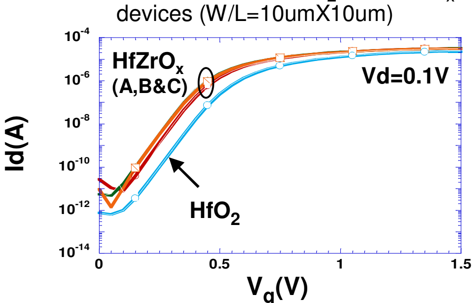

Fig. 8 Id-Vg characteristics of $HfZrO_x$ NMOSFET(W/L=10umX10um)

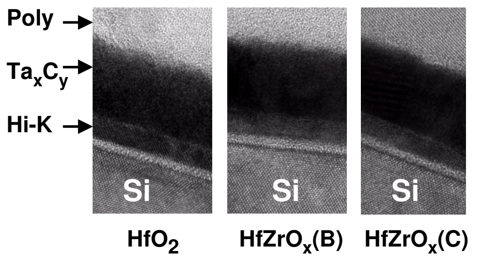

Fig. 9 XTEM images of $HfZrO_x$ NMOSFETs showing good thermal stability with Si

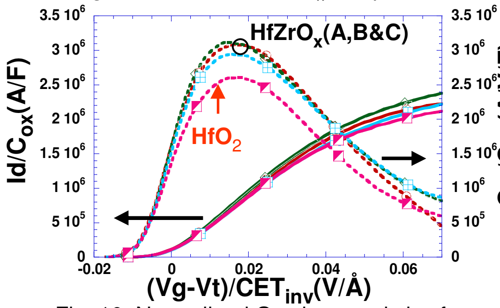

Fig. 10 Normalized G_m characteristics for $HfZrO_x$ devices(W/L=10µmX10µm)

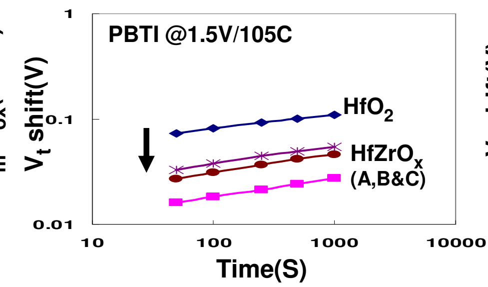

Fig. 11 V_t instability with electrical stress for $HfZrO_x$ NMOSFET(W/L=10µmX10µm)

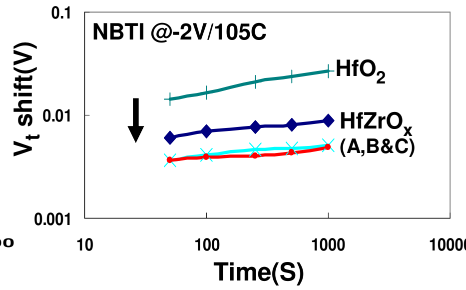

Fig. 12 V_t instability with electrical stress for $HfZrO_x$ PMOSFET(W/L=10µmX10µm)

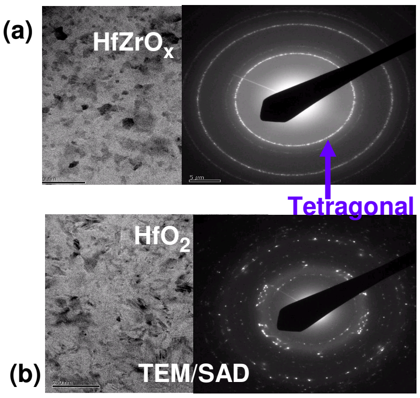

Fig. 13 plan view TEM and SAD of (a)$HfZrO_x$ and (b)HfO_2 films

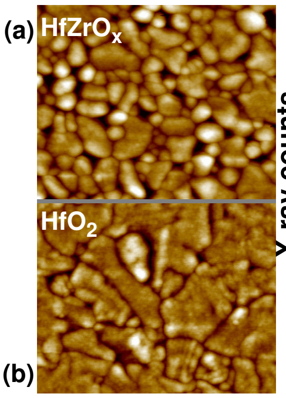

Fig. 14 AFM images of (a)$HfZrO_x$ and (b)HfO_2 films

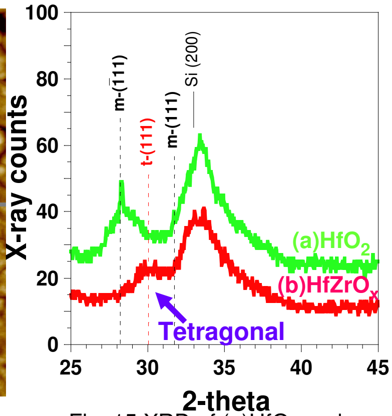

Fig. 15 XRD of (a)HfO_2 and (b)$HfZrO_x$ films

Table I

$HfZrO_x$ NMOSFET results*

High-K	CET_{inv}(Å)	V_t(V)	SS(mV/dec)
$HfZrO_x$(A)	15.7	0.39	66
$HfZrO_x$(B)	15.6	0.37	67
$HfZrO_x$(C)	15.1	0.38	67
HfO_2	17.5	0.44	68

(*long channel devices using shorter flow)